

Mechanism of the fcc-to-hcp phase transformation in solid Ar

Bingxi Li, Guangrui Qian, Artem R. Oganov, Salah Eddine Boufelfel, and Roland Faller

Citation: *The Journal of Chemical Physics* **146**, 214502 (2017); doi: 10.1063/1.4983167

View online: <http://dx.doi.org/10.1063/1.4983167>

View Table of Contents: <http://aip.scitation.org/toc/jcp/146/21>

Published by the [American Institute of Physics](#)

Articles you may be interested in

[First-principles investigation of Zr-O compounds, their crystal structures, and mechanical properties](#)
Journal of Applied Physics **121**, 155104 (2017); 10.1063/1.4979913

[Thermophysical properties of krypton-helium gas mixtures from ab initio pair potentials](#)
The Journal of Chemical Physics **146**, 214302 (2017); 10.1063/1.4984100

[Self-intermediate scattering function analysis of supercooled water confined in hydrophilic silica nanopores](#)
The Journal of Chemical Physics **146**, 214501 (2017); 10.1063/1.4984764

[On the physical interpretation of the nuclear molecular orbital energy](#)
The Journal of Chemical Physics **146**, 214103 (2017); 10.1063/1.4984098

[Electron-phonon coupling in anthracene-pyromellitic dianhydride](#)
The Journal of Chemical Physics **146**, 214705 (2017); 10.1063/1.4984268

[On extending Kohn-Sham density functionals to systems with fractional number of electrons](#)
The Journal of Chemical Physics **146**, 214109 (2017); 10.1063/1.4982951



**COMPLETELY
REDESIGNED!**

**PHYSICS
TODAY**

Physics Today Buyer's Guide
Search with a purpose.

Mechanism of the fcc-to-hcp phase transformation in solid Ar

Bingxi Li,^{1,a)} Guangrui Qian,² Artem R. Oganov,^{3,2,4,5} Salah Eddine Boulfelfel,⁶ and Roland Faller^{7,b)}

¹Department of Materials Science and Engineering, University of California, Davis, California 95616, USA

²Department of Geosciences, Stony Brook University, Stony Brook, New York 11794, USA

³Skolkovo Institute of Science and Technology, Skolkovo Innovation Center, 5 Nobel St., Moscow 143026, Russia

⁴Moscow Institute of Physics and Technology, Dolgoprudny, Moscow Region 141700, Russia

⁵International Center for Materials Design, Northwestern Polytechnical University, Xi'an 710072, China

⁶School of Chemical and Biomolecular Engineering, Georgia Institute of Technology, Atlanta, Georgia 30332, USA

⁷Department of Chemical Engineering, University of California, Davis, California 95616, USA

(Received 30 October 2016; accepted 26 April 2017; published online 6 June 2017)

We present an atomistic description of the *fcc*-to-*hcp* transformation mechanism in solid argon (Ar) obtained from transition path sampling molecular dynamics simulation. The phase transition pathways collected during the sampling for an 8000-particle system reveal three transition types according to the lattice deformation and relaxation details. In all three transition types, we see a critical accumulation of defects and uniform growth of a less ordered transition state, followed by a homogeneous growth of an ordered phase. Stacking disorder is discussed to describe the transition process and the cooperative motions of atoms in {111} planes. We investigate nucleation with a larger system: in a system of 18 000 particles, the collective movements of atoms required for this transition are facilitated by the formation and growth of stacking faults. However, the enthalpy barrier is still far beyond the thermal fluctuation. The high barrier explains previous experimental observations of the inaccessibility of the bulk transition at low pressure and its sluggishness even at extremely high pressure. The transition mechanism in bulk Ar is different from Ar nanoclusters as the orthorhombic intermediate structure proposed for the latter is not observed in any of our simulations. *Published by AIP Publishing.* [<http://dx.doi.org/10.1063/1.4983167>]

I. INTRODUCTION

Rare gas solids (RGSs) of neon, argon, krypton, and xenon crystallize in face-centered cubic (*fcc*) structures at ambient pressure and low temperatures.^{1,2} However, early experimental studies and theoretical predictions pointed out the possibility of a hexagonally close-packed (*hcp*) structure.^{3–7} The *hcp* structure can coexist with *fcc* as a metastable phase in pure rare gas solids at low temperatures^{3–6} and becomes stable in solid solutions.^{3,8,9} Calculations based on two- and many-body interaction potentials have predicted the *hcp* structure to be energetically more favorable than the *fcc* polymorph.^{10,11} This stability order is reversed after including zero-point vibrational effects.¹⁰

Even though the stability of *fcc* and *hcp* phases under ambient pressure has been disputed for decades, the stability of *hcp* structures is evidenced by many high-pressure experiments.^{12–18} Rare gas solids martensitically transform from *fcc* to *hcp* before metallization occurs under pressure.^{12–15} However, the pressure-induced *fcc*-to-*hcp* transition in RGSs is rather sluggish and the two phases coexist over a wide range of pressures. X-ray diffraction and Raman spectroscopy show

a transformation pressure in the range between 1.5–41 and 3.2–50 GPa for Xe and Kr, respectively, and beyond 49.6 GPa for Ar.^{12–14,16–18} Theoretically, sluggishness of the *fcc* to *hcp* transformation in Xe was attributed to a high energy barrier.¹⁹ A first-principles study determined the enthalpy barrier for a stacking disorder growth pathway²⁰ at lower pressure and an alternative pathway involving an orthorhombic distortion at higher pressure.

Recent theoretical and experimental studies^{21–23} investigated the phase behavior of Ar clusters under ambient pressure. It was shown that increasing the Ar cluster size led to a transition from *fcc* to *fcc/hcp* mixed structures during cluster growth. An orthorhombic structure was predicted as intermediate in the *fcc*-to-*hcp* transition as it accounts for the diffraction peaks originating from neither in *fcc* nor *hcp* structures in Ar nanoclusters.^{24,25} Although the *fcc*-to-*hcp* transition mechanism was well studied for rare gas clusters, a comprehensive understanding of this transformation in the corresponding bulk materials is still elusive.

Molecular dynamics is a powerful method for mechanistic investigations. However, the existence of a high enthalpy barrier of transition greatly reduces the efficiency of finding the transition path. The transition path sampling^{26,27} method is designed to solve this problem. Therefore, we employ transition path sampling to provide a detailed atomistic understanding of the transition mechanism.

^{a)}bxli@ucdavis.edu

^{b)}rfaller@ucdavis.edu

II. TRANSITION PATH SAMPLING

This section briefly reviews transition path sampling (TPS)^{26,27} for transition pathways with deterministic dynamics.²⁸ Besides, we present the identification of the initial and final state of transition pathways using a fingerprint function.²⁹ The characterization of structures formed during transition is also discussed.

A. Transition path sampling

TPS performs importance sampling in a transition path ensemble with two main trial moves, shooting and shifting.

A shooting move randomly chooses a time slice of a trajectory and adds a perturbation δp drawn from a Gaussian distribution to its atomic momenta. The selected time slice $x_t^{(o)}$ at time t on the old path will yield a new phase space point $x_t^{(n)}$ as the starting point for a new trajectory. A new trajectory with time length being T is generated by shooting forward to time T and backward to time 0 from time t . For deterministic dynamics, the acceptance probability of this move is

$$P_{acc}^{o \rightarrow n} = h_A[x_0^{(n)}]h_B[x_T^{(n)}] \min \left[1, \frac{\rho(x_t^{(n)})}{\rho(x_t^{(o)})} \right], \quad (1)$$

where $\rho(x_t^{(o)})$ and $\rho(x_t^{(n)})$ are the equilibrium phase space distribution of the old and new time slices at time t , respectively. $h_A[x_0^{(n)}]$ has a binary value 1 for the beginning structure of the new trajectory, $x_0^{(n)}$, in state A and 0 otherwise. $h_B[x_T^{(n)}]$ is defined equivalently for the ending structure of the new trajectory, $x_T^{(n)}$.

A shifting move translates the old trajectory by a time shift Δt that can be drawn from a Gaussian distribution. The corresponding acceptance probability $P_{acc}^{o \rightarrow n}$ is

$$P_{acc}^{o \rightarrow n} = h_A[x_0^{(n)}]h_B[x_T^{(n)}]. \quad (2)$$

The initial trajectory connecting the initial and final state which is needed to start transition path sampling simulations was generated by the variable-cell nudged elastic band³⁰ method. For the following transition path sampling molecular dynamics simulations, we used the TPS module from the USPEX package.^{31–34} In the TPS simulation of the system of 8000 Ar atoms, 7427 distinct trajectories were created by 17 334 shooting and shifting moves during the sampling. In a larger system of 18 000 Ar atoms, 8688 trajectories were sampled after 20 410 shooting and shifting moves.

B. Molecular dynamics simulation

Classical molecular dynamics simulations are carried out using the LAMMPS code³⁵ to generate the new trajectories after each shooting or shifting move. The velocity-Verlet algorithm with an integration time step of 0.1 fs is used to ensure time-reversibility. The simulation employed a Nose–Hoover thermostat³⁶ with a relaxation time of 30 fs and a Nose–Hoover barostat³⁷ with a relaxation time of 300 fs, ensuring an NpT ensemble at $T = 40$ K and $p = 1$ bar.²⁵ The simulation box containing 8000 or 18 000 Ar atoms allows anisotropic shape changes to avoid biasing the evolution of the dynamics and the resulting transition mechanism.

The interatomic interactions were modeled using a Lennard–Jones (LJ) 12–6 model with Ar interaction parameters $\sigma = 3.405$ Å and $\epsilon = 0.238$ kcal/mol^{10,38} and truncated at 10 Å. The LJ potential has been widely applied to study rare gas solids, e.g., their melting.^{10,39}

C. Characterization of structures

Structures encountered during the phase transition may have low or even no crystallinity. To characterize these transitory structures, we compute the structure similarity function and coordination numbers to analyze their lattice deformation and the local packing.

The structure similarity value is used as the order parameter to measure the phase transition boundary. It refers to the cosine similarity between the fingerprint vectors of different structures.²⁹ Each structure is represented by a fingerprint vector generated by the values of its fingerprint function $f_x(r)$ in each bin (of width Δ).

The fingerprint function $f(r)$ subtracts 1 from the radial distribution function (RDF) and is short-ranged. The fingerprint vector F is obtained through its discretization. Each structure is therefore described as a vector in the fingerprint space, the dimensionality of which equals the number of discretization bins. For a structure x during the phase transition, the fingerprint vector F_x can be written as

$$F_x = [f_x(r_0), f_x(r_1), \dots, f_x(r_n)] \\ = [g_x(r_0) - 1, g_x(r_1) - 1, \dots, g_x(r_n) - 1], \quad (3)$$

where $g_x(r)$ is the RDF value of structure x at distance r . Our structure similarity function measures similarity between structures by calculating the cosine similarity in fingerprint space. The similarity of structure x to the *fcc* phase is then determined using the structure similarity function $S_{fcc}(x)$,

$$S_{fcc}(x) = \frac{\vec{F}_x \cdot \vec{F}_{fcc}}{|\vec{F}_x| |\vec{F}_{fcc}|}, \quad (4)$$

which is the cosine similarity between the fingerprint vector of structure x and the *fcc* phase. The structure similarity function ranges from 0, meaning totally different, to 1, meaning identical; in-between values indicate intermediate similarity. In this paper, the *fcc*-structure similarity criterion is set to be 0.999, i.e., if $S_{fcc} \geq 0.999$, we identify a structure as *fcc*. The similarity to the *hcp* phase is defined analogously. Structures with $S_{fcc} < 0.999$ and $S_{hcp} < 0.999$ are regarded as transitory structures. Transitory structures define the transition region for each trajectory.

By comparing the percentages of differently coordinated atoms in each transitory structure, we can develop a view into the local packing changes during phase transition. The coordination number is computed as the number of neighbor atoms within the specified cutoff distance from the central atom. The cutoff distance is placed on the first local minimum of the RDF of each structure. The cutoff varies from structure to structure along the trajectory. The first minimum is at the shortest distance for crystalline structures and at larger distances for

intermediate structures. The first local minimum is the same for the two close-packed structures. In *fcc* and *hcp* structures, the coordination number of each atom is 12, equal to the number of nearest neighbors. Over- and under-coordinated atoms appear during the transition.

III. RESULTS

A. Small system

We first discuss the 8000-particle system. Through transition path sampling molecular dynamics simulation, we developed an atomistic understanding of *fcc*-to-*hcp* phase transformation in Ar solid at 40 K under ambient pressure. The transition pathways are categorized into three types according to the lattice deformation and relaxation details. But all three types of transitions go through the same enthalpy barrier. The barrier is 578 ± 50 kcal/mol for the *fcc* \rightarrow *hcp* transition in Ar solid modeled by a system of 8000 atoms, which is far beyond the thermal energy at 40 K ($kT = 0.0795$ kcal/mol).

1. Three types of transition pathways

We are defining 3 types of transitions. Trajectory I represents the type I transition. The structure deforms slowly from the *fcc* phase to the transition state but relaxes quickly to the *hcp* phase. The growth and decay rates of local defects dominate the transformation process. Figs. 1(b) and 1(c) indicate the consistency between the lattice deformation and local defects. When more than 1.5% of atoms become over- or under-coordinated, the lattice loses its similarity to *fcc* at 2.81 ps. According to Figs. 1(a) and 1(c), the increasing enthalpy follows the local packing change from the beginning of transition. When the system reaches the local minimum in enthalpy at 6.25 ps, over 80% atoms are not 12-coordinate. After waiting for sufficient thermal fluctuations to activate further local packing changes, more local defects are generated to accelerate the lattice deformation. When the system has the highest enthalpy and largest number of local defects at 6.94 ps, the structure has least similarity to both *fcc* and *hcp* phase. 99.83% atoms become over-coordinated. More details on the crystallinity of intermediate states are presented in the [supplementary material](#). The lattice afterwards quickly relaxes to the *hcp* phase. Although the average arrangement of atoms first demonstrates the character of *hcp* at 8.67 ps, the coordination numbers still stabilize to 12 until 9.69 ps in order to dissipate the energy fluctuations.

A type II transition can be observed in trajectory II (Fig. 2). During the transition, the lattice deformation and relaxation take almost equal time. Based on the structure similarity, the lattice begins to deform at 1.74 ps and reaches the largest deformation 5.29 ps later. Then it takes 4.63 ps to relax into the *hcp* phase. As shown in Fig. 2(a), two metastable states appear during the lattice deformation and relaxation. The first metastable state forms at 6.39 ps and soon accumulates thermal energy to produce more local defects, which facilitate the following lattice deformation. After overcoming the transition saddle at 7.03 ps, the system is trapped into a second metastable state. It just takes 0.39 ps to overcome the

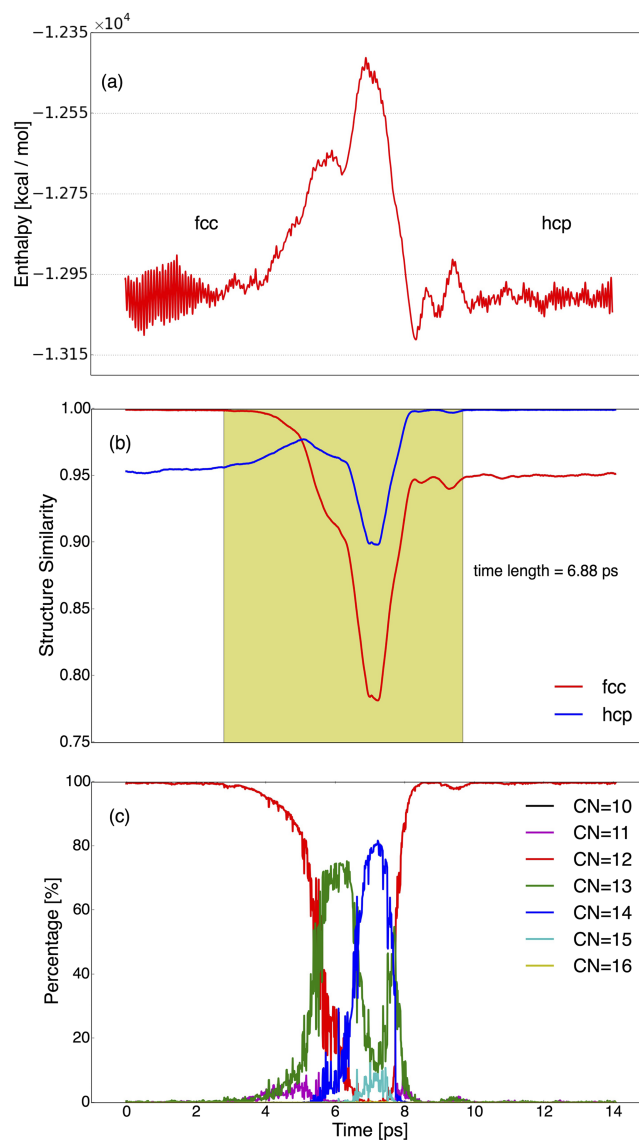


FIG. 1. (a) Enthalpy along trajectory I. (b) The transition region (yellow) of trajectory I. Structure similarities to *fcc* and *hcp* phases are plotted in red and blue. (c) The percentages of atoms with different coordination numbers along trajectory I.

small enthalpy barrier and finally relax to the *hcp* phase at 11.66 ps.

Fig. 3 indicates a type III transition, in which the lattice experiences a fast deformation and slow relaxation. Starting with a small thermal fluctuation at 4.45 ps, only 1.5% of atoms become not-12-coordinate until 5.56 ps. The structure still keeps 99.8% similarity to *fcc*. However, induced by a large fluctuation at that point, the lattice experiences a rapid change. 99.87% of atoms become over-coordinated within 1.7 ps. As a result, the transition state has the largest deformation from both *fcc* and *hcp* phases at 7.26 ps. A following increase of 12-coordinate atoms reduces the local defects and leads to a metastable phase with more structural similarity to *hcp* phase at 7.91 ps. Another 0.51 ps is required to overcome the enthalpy barrier. The relaxation to *hcp* is completed at 13.36 ps. The whole transition as characterized by structure similarity takes 8.91 ps.

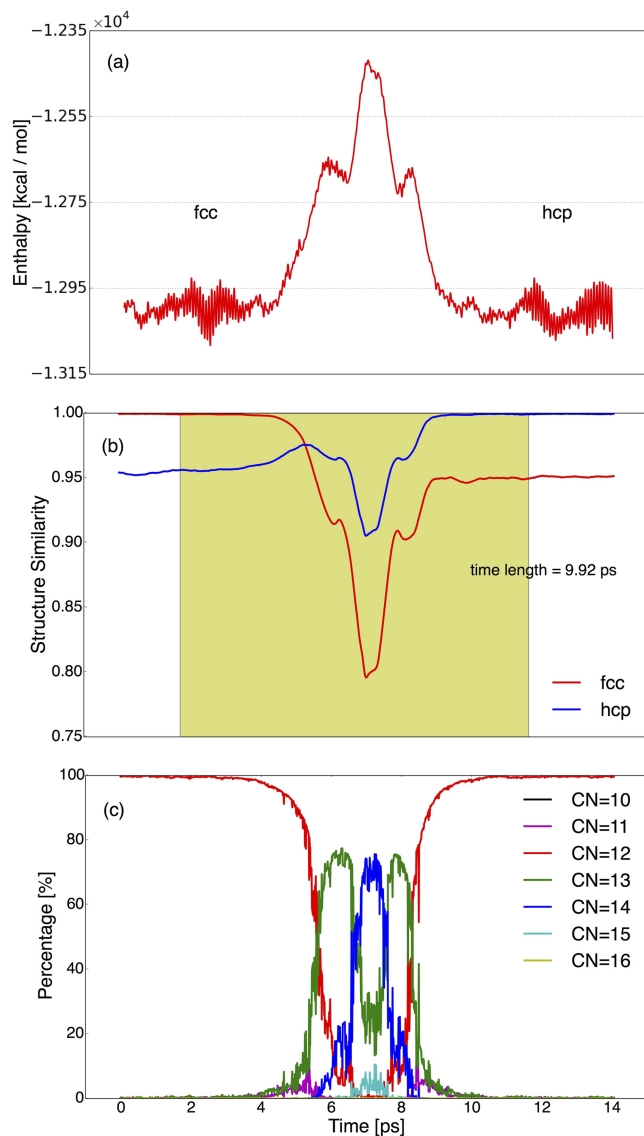


FIG. 2. (a) Enthalpy along trajectory II. (b) The transition region (yellow) of trajectory II. Structure similarities to *fcc* and *hcp* phases are plotted in red and blue. (c) The percentages of atoms with different coordination numbers along trajectory II.

Looking at the enthalpy profiles along the three transformation paths, we see that their activation enthalpies are very close to each other. From an enthalpy viewpoint alone one could conclude that these paths have equal chances to occur, but this would ignore entropy effects. A simple way to judge the likelihood of occurrence of each path, taking entropy into account, is to count the frequency of occurrence of each type of pathway. We find that the percentage of type I is 25.6%, type II is 13.0%, and type III is 61.4%. We therefore assume that type III is the most likely but the other ones have a significant share.

Despite the difference in lattice deformation and relaxation, the three types of transition all go through less ordered intermediates at this small system size. The order of the intermediate state is between fully amorphous and a crystalline solid. These intermediate structures are dominated by over-coordinated atoms, most of which are 13- and 14-coordinate. It is noticeable that the intermediate structure in type III

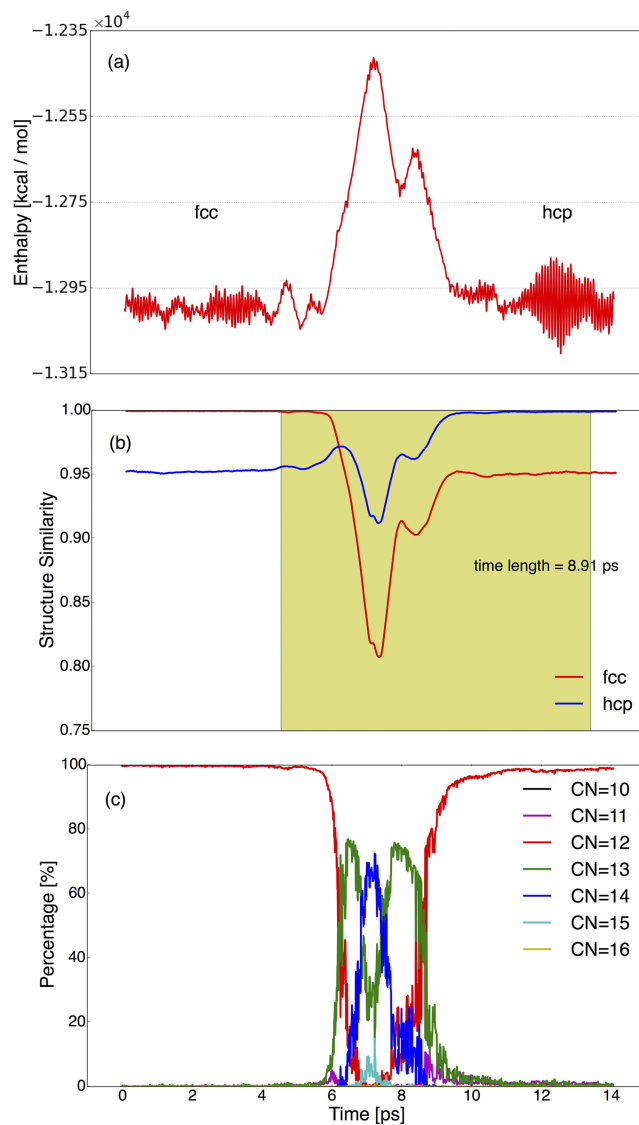


FIG. 3. (a) Enthalpy along trajectory III. (b) The transition region (yellow) of trajectory III. Structure similarities to *fcc* and *hcp* phases are plotted in red and blue. (c) The percentages of atoms with different coordination numbers along trajectory III.

transition has the highest similarity to *fcc* and *hcp* phases. Therefore less structural deformation is required in this type of transition.

2. Transition mechanism

In Fig. 4, we observe the phase growth along trajectory I. At the beginning, nearly all atoms in the *fcc* structure are 12-coordinate. The lattice is characterized by a stacking sequence $\dots ABCABC\dots$. More than 80% atoms remain 12-coordinate when the lattice starts to deform at 2.81 ps. Then some 13-coordinate atoms appear and distribute uniformly throughout the lattice. These 13-coordinate atoms form a metastable phase at 6.25 ps and further transform into another intermediate, which is mainly dominated by 14-coordinate atoms. At 6.94 ps, 99.83% of atoms become 14-coordinate. When the lattice begins to relax from the largest deformation as shown in Fig. 1(b), 12-coordinate atoms grow homogeneously within the cell. The lattice finally relaxes to *hcp* by 8.67 ps. The

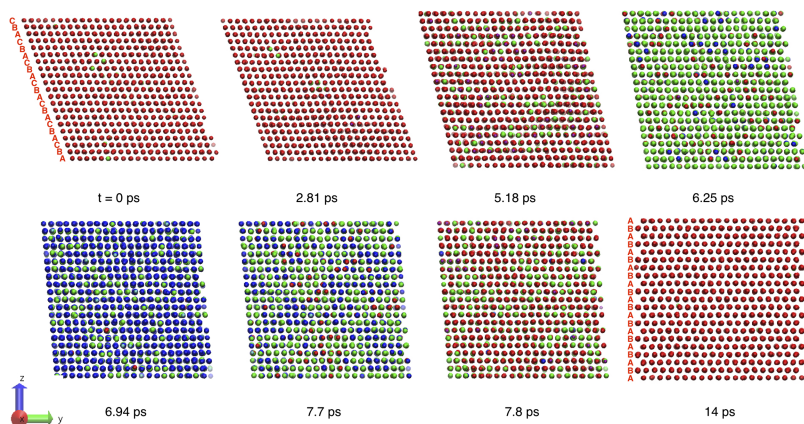


FIG. 4. Snapshots of configurations during a transition in 8000-particle system, different colors are different coordination numbers. Atoms shown by red are 12-coordinate while green and blue are for 13- and 14-coordinate atoms.

whole system ends with the *hcp* phase at 14 ps with a stacking sequence of $\dots ABABAB \dots$. Fig. 5 illustrates details of the volume change of the cell shown in Fig. 4. There is 2.59% expansion of the cell during the phase transition. The consistencies of volume change with enthalpy, structure similarity, and coordinates are explained in the [supplementary material](#).

Fig. 4 shows the homogeneous growth of the intermediate and the new ordered phase during the *fcc-to-hcp* transition in Ar solid. Through the collective sliding of planes, accompanied by the formation of defects, stacking sequence changes from $\dots ABCABC \dots$ in *fcc* to $\dots ABABAB \dots$ in *hcp*. The cooperative movement of many atoms not only results in the *fcc* stacking growth into *hcp* domains but also leads to the lattice deformation. This explains the consistency between lattice deformation and local packing shown in Fig. 1. The stacking disorder growth mechanism is also observed in two other models of phase transition. This mechanism was previously observed in experimental studies of *fcc-to-hcp* transition in Xe and Kr.^{13,20} A first-principles calculation suggested this mechanism as the transition pathway in Xe at lower pressure.¹⁹ An X-ray diffraction study on solid Ar up to 114 GPa predicted the development of stacking disorder during the transition.¹⁴ Our results on the high enthalpy barrier explain the inaccessibility of this transition in bulk at low pressure. A recent study on *fcc-to-hcp* transition in Ar cluster at ambient pressure observes an orthorhombic intermediate²⁵ while our stacking disorder growth mechanism in bulk Ar suggests a less ordered intermediate mainly due to

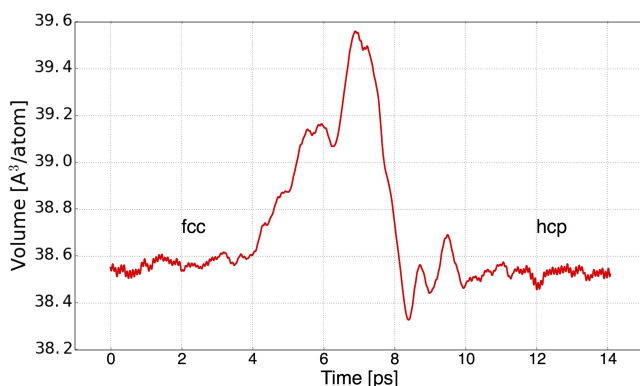


FIG. 5. Volume change in a type I trajectory.

the high appearance of defects in parallel to the sliding. The system generates such a high density of defects throughout so that it appears no longer crystalline.

B. Large system

As we did not observe nucleation in our 8000-particle system, which is peculiar for a system undergoing a first-order transition, we performed simulations in a system with 18 000 particles using the same approach as before. The enthalpy barrier for the 18 000-particle system turns out to be 826 ± 49 kcal/mol. Here we find its enthalpy barrier per particle to be smaller than in the 8000-particle system (see Fig. 6) indicating that not the whole system is transitioning homogeneously at the same time, i.e., we see nucleation events. This is consistent with the findings by inspecting individual transitions. The maximum deviation from both *hcp* and *fcc* structures in the fingerprint function is weaker than that in the smaller system. The structure similarity of a representative trajectory in large system is given in Fig. 7(a) as an example. The higher similarity to *hcp* and *fcc* structures of intermediate state shows that in contrast to the smaller system, the large system does not completely lose the old structure before rebuilding the new one. Also the overall volume expansion during the transition is not as pronounced (Fig. 7(b)). It actually turns out that both the 8000- and 18 000-particle systems have a very similar absolute

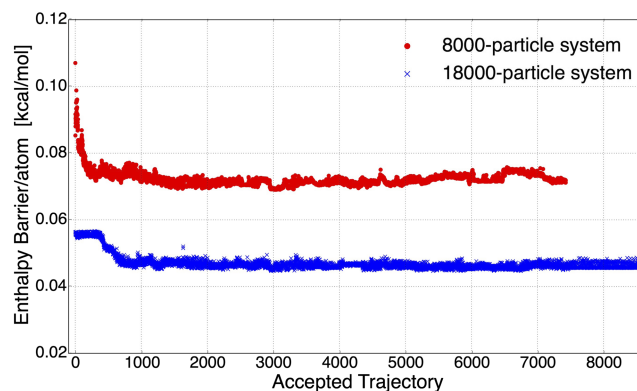


FIG. 6. Enthalpy barriers for 8000- and 18 000-particle system as a function of successful TPS trajectories. Not all the initial energies are shown due to limitations on the vertical scale. The enthalpy barrier per atom of the first trajectory in 8000-particle and 18 000-particle TPS simulations are 0.849 kcal/mol and 0.533 kcal/mol (normalized per atom), respectively.

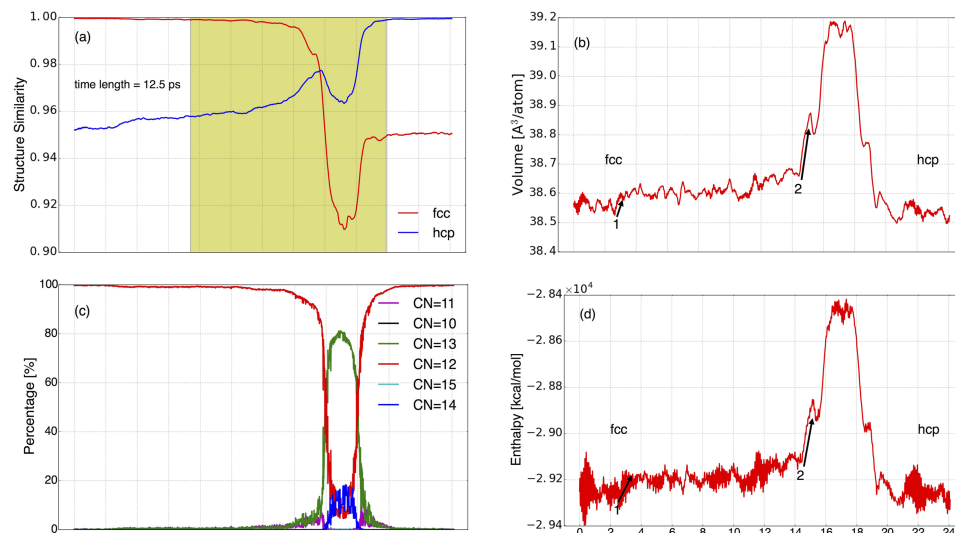


FIG. 7. A representative trajectory in 18000-particle system shows (a) structure similarities to *fcc* and *hcp* phases are plotted in red and blue, (b) atomic volume, (c) percentages of atoms with different coordination numbers, and (d) enthalpy during *fcc*-to-*hcp* transition.

maximum volume change. This suggests that the 8000 particle system discussed above captures some features of the real mechanism, yet we need a large system to be able to have some decorrelation in space necessary for nucleation. In Fig. 7(c), we also find that with 18 000 particles, there is a small but not negligible portion of 12-coordinate atoms visible at all times in contrast to smaller system of 8000 particles above.

If we look at visualizations of a transition in Fig. 8, it appears that the nucleation mentioned above is actually the formation and growth of stacking fault followed by the growth of the new phase through $\{111\}$ plane sliding. The system has the stacking sequence of $\dots ABCABC\dots$ along the $\langle 111 \rangle$ direction at the beginning of the transition. After

3.19 ps, some defects are created locally in the system and they evolve into a stacking fault. The stacking sequence changes from $\dots ABCABCABC\dots$ to $\dots ABCAABCAB\dots$ in the circled region at 6.97 ps. During the formation of this stacking fault, we notice increases in both enthalpy and atomic volume, which are marked by arrow 1 in Figs. 7(b) and 7(d). Disorder is then created at one side of the stacking fault and its propagation yields another two stacking faults across the system at 14.64 ps. More stacking faults are generated before the collective movement of atoms in the whole system starts. They are marked with arrows in Fig. 8(f). The growth of stacking faults is also indicated by rapid increases in enthalpy and atomic volume (arrow 2 in Figs. 7(b) and 7(d)). With these stacking

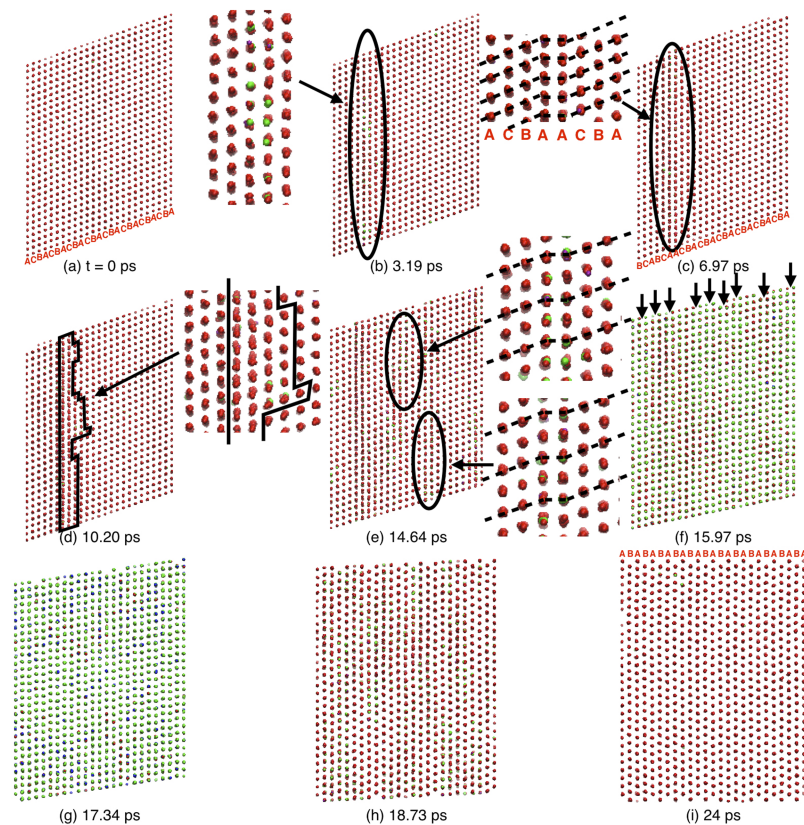


FIG. 8. Snapshots of configurations during a transition in 18 000-particle system, different colors are different coordination numbers. Atoms in red are 12-coordinate while green and blue are for 13- and 14-coordinate atoms. Individual labels (a)-(i) denote the time along the trajectory. (a): Before transition, (b)-(e): nucleus during transition, (f)-(h): growth of stacking faults and new ordered phase during transition, (i): after transition.

faults, the transition is then carried on by the sliding of {111} planes, which involves locally cooperative motions of atoms. In the most deformed state, more than 90% atoms become over-coordinated. The 12 coordinates are regained for 90% atoms at 18.73 ps, after which the system gradually relaxes into *hcp* state.

There are only quantitative differences between small and large system, e.g., barrier heights. The transition in the 18 000-particle system experiences the formation and growth of stacking faults over the system. The stacking faults facilitate the locally collective movement of atoms. Despite the assistance of stacking faults, the enthalpy barrier is still far beyond the thermal fluctuations at 40 K.

IV. CONCLUSIONS

Our results show that *fcc*-to-*hcp* transformation in solid Ar at 40 K under ambient pressure is completed through the collective sliding of {111} planes in *fcc* structure which generates a high defect density. The system needs a large coherent volume for this transition such that only in our large 18 000-atom system we find nucleation. The stacking sequence experiences disorder during its transition from ...*ABCABC*... in *fcc* to ...*ABABAB*... in *hcp*. Unlike the transition in Ar clusters,²⁵ no mechanism through an orthorhombic intermediate is observed. Instead we observe an intermediate state of lower order formed by 13- and 14-coordinate atoms in all three types of transition of the small system. The inaccessibility of *fcc*-to-*hcp* transformation in bulk Ar under low pressure and its sluggishness under high pressure^{12–18,21–25} can be explained by our results on the transition enthalpy barrier, which is far beyond the thermal fluctuation. The formation and growth of stacking faults in the large system facilitate the transition.

The TPS method employed in our research provides an atomistic understanding of the Ar phase transition. Our results explain the inaccessibility and sluggishness of this transition in experiments and predict a different intermediate.

It is possible that with even larger systems, the transition localizes further. It would be interesting to perform (presently hardly affordable) TPS simulations on even larger systems in order to explore the nucleation event.

SUPPLEMENTARY MATERIAL

See [supplementary material](#) for the first minimum of RDFs used as cutoff distance to compute coordination numbers of atoms in the structures of all trajectories. The correlations of volume changes with enthalpy, structure similarity, and coordinates are also discussed. Besides we employ structure function to investigate the crystallinity of the intermediate states in two systems of different size.

¹T. H. K. Barron and C. Domb, in *Proceedings of the Royal Society A: Mathematical, Physical and Engineering Sciences* (The Royal Society, 1955) pp. 447–465.

²L. Jansen, *Phys. Lett.* **4**, 91–94 (1963).

- ³L. Meyer, C. S. Barrett, and P. Haasen, *J. Chem. Phys.* **40**, 2744–2745 (1964).
- ⁴C. S. Barrett and L. Meyer, *J. Chem. Phys.* **41**, 1078–1081 (1964).
- ⁵E. Schubert, M. Creuzburg, and W. Müller-Lierheim, *Phys. Status Solidi B* **76**, 301–306 (1976).
- ⁶Y. Sonnenblick, E. Alexander, Z. Kalman, and I. Steinberger, *Chem. Phys. Lett.* **52**, 276–278 (1977).
- ⁷B. W. van de Waal, *Phys. Rev. Lett.* **67**, 3263–3266 (1991).
- ⁸N. N. Gal'tsov, A. I. Prokhvatilov, and M. A. Strzhemechnyĭ, *Low Temp. Phys.* **30**, 984–989 (2004).
- ⁹A. E. Curzong and M. J. Eastell, *J. Phys. C: Solid State Phys.* **4**, 689 (1971).
- ¹⁰P. Schwerdtfeger, N. Gaston, R. P. Krawczyk, R. Tonner, and G. E. Moyano, *Phys. Rev. B* **73**, 064112 (2006).
- ¹¹N. V. Krainyukova, *Low Temp. Phys.* **37**, 435–438 (2011).
- ¹²D. Errandonea, B. Schwager, and R. Boehler, *High Pressure Res.* **22**, 375–379 (2002).
- ¹³D. Errandonea, B. Schwager, R. Boehler, and M. Ross, *Phys. Rev. B* **65**, 214110 (2002).
- ¹⁴D. Errandonea, R. Boehler, S. Japel, M. Mezouar, and L. R. Benedetti, *Phys. Rev. B* **73**, 092106 (2006).
- ¹⁵A. P. Jephcoat, H. K. Mao, L. W. Finger, D. E. Cox, R. J. Hemley, and C. S. Zha, *Phys. Rev. Lett.* **59**, 2670–2673 (1987).
- ¹⁶H. Shimizu, N. Wada, T. Kume, S. Sasaki, Y. Yao, and J. S. Tse, *Phys. Rev. B* **77**, 052101 (2008).
- ¹⁷Y. A. Freiman, A. F. Goncharov, S. M. Tretyak, A. Grechnev, J. S. Tse, D. Errandonea, H.-K. Mao, and R. J. Hemley, *Phys. Rev. B* **78**, 014301 (2008).
- ¹⁸H. Shimizu, M. Kawajiri, T. Kume, S. Sasaki, Y. A. Freiman, and S. M. Tretyak, *Phys. Rev. B* **79**, 132101 (2009).
- ¹⁹E. Kim, M. Nicol, H. Cynn, and C.-S. Yoo, *Phys. Rev. Lett.* **96**, 035504 (2006).
- ²⁰H. Cynn, C. S. Yoo, B. Baer, V. Iota-Herbei, A. K. McMahan, M. Nicol, and S. Carlson, *Phys. Rev. Lett.* **86**, 4552–4555 (2001).
- ²¹O. G. Danylchenko, S. I. Kovalenko, and V. N. Samovarov, *Low Temp. Phys.* **30**, 166–170 (2004).
- ²²A. G. Danilchenko, S. I. Kovalenko, and V. N. Samovarov, *Low Temp. Phys.* **34**, 966–968 (2008).
- ²³O. G. Danylchenko, S. I. Kovalenko, O. P. Konotop, and V. N. Samovarov, *Low Temp. Phys.* **40**, 1083–1086 (2014).
- ²⁴E. T. Verkhovtseva, I. A. Gospodarev, A. V. Grishaev, S. I. Kovalenko, D. D. Solnyshkin, E. S. Syrkin, and S. B. Feodosev, *Low Temp. Phys.* **29**, 386–393 (2003).
- ²⁵N. V. Krainyukova, R. E. Boltnev, E. P. Bernard, V. V. Khmel'enko, D. M. Lee, and V. Kiryukhin, *Phys. Rev. Lett.* **109**, 245505 (2012).
- ²⁶P. G. Bolhuis, D. Chandler, C. Dellago, and P. L. Geissler, *Annu. Rev. Phys. Chem.* **53**, 291–318 (2002).
- ²⁷C. Dellago, P. G. Bolhuis, and P. L. Geissler, *Computer Simulations in Condensed Matter Systems: From Materials to Chemical Biology* (Springer, 2006), pp. 349–391.
- ²⁸P. G. Bolhuis, C. Dellago, and D. Chandler, *Faraday Discuss.* **110**, 421–436 (1998).
- ²⁹A. R. Oganov and M. Valle, *J. Chem. Phys.* **130**, 104504 (2009).
- ³⁰G.-R. Qian, X. Dong, X.-F. Zhou, Y. Tian, A. R. Oganov, and H.-T. Wang, *Comput. Phys. Commun.* **184**, 2111–2118 (2013).
- ³¹C. W. Glass, A. R. Oganov, and N. Hansen, *Comput. Phys. Commun.* **175**, 713–720 (2006).
- ³²A. R. Oganov, A. O. Lyakhov, and M. Valle, *Acc. Chem. Res.* **44**, 227–237 (2011).
- ³³A. O. Lyakhov, A. R. Oganov, H. T. Stokes, and Q. Zhu, *Comput. Phys. Commun.* **184**, 1172–1182 (2013).
- ³⁴S. E. Boulfelfel, A. R. Oganov, and S. Leoni, *Sci. Rep.* **2**, 471 (2012).
- ³⁵S. Plimpton, *J. Comput. Phys.* **117**, 1–19 (1995).
- ³⁶W. G. Hoover, *Phys. Rev. A* **31**, 1695–1697 (1985).
- ³⁷W. G. Hoover, *Phys. Rev. A* **34**, 2499–2500 (1986).
- ³⁸J. Hirschfelder, C. Curtis, and R. Bird, *The Molecular Theory of Gases and Liquids* (Wiley, New York, 1964).
- ³⁹L. Gómez, C. Gazza, H. Dacharry, L. Peñaranda, and A. Dobry, *Phys. Rev. B* **71**, 134106 (2005).